ADVANCED MATERIALS

Supporting Information

for *Adv. Mater.*, DOI: 10.1002/adma.201703435

Realization of Large Electric Polarization and Strong Magnetoelectric Coupling in $BiMn_3Cr_4O_{12}$

*Long Zhou, Jianhong Dai, Yisheng Chai, Huimin Zhang, Shuai Dong, Huibo Cao, Stuart Calder, Yunyu Yin, Xiao Wang, Xudong Shen, Zhehong Liu, Takashi Saito, Yuichi Shimakawa, Hajime Hojo, Yuichi Ikuhara, Masaki Azuma, Zhiwei Hu, Young Sun, Changqing Jin, and Youwen Long**

Supporting Information

Realization of Large Electric Polarization and Strong Magnetoelectric Coupling in $BiMn_3Cr_4O_{12}$

*Long Zhou, Jianhong Dai, Yisheng Chai, Huimin, Zhang, Shuai Dong, Huibo Cao, Stuart Calder, Yunyu Yin, Xiao Wang, Xudong Shen, Zhehong Liu, Takashi Saito, Yuichi Shimakawa, Hajime Hojo, Yuichi Ikuhara, Masaki Azuma, Zhiwei Hu, Young Sun, Changqing Jin, and Youwen Long**

Experimental and theoretical section

Sample synthesis: The polycrystalline $BiMn_3Cr_4O_{12}$ was prepared by a high-pressure and high-temperature method. The highly pure (> 99.9%) Bi_2O_3, Mn_2O_3 and Cr_2O_3 powders were used as starting materials. The finely mixed reactants with stoichiometric composition were packed into a gold capsule and then treated at 8 GPa and 1373 K for 30 min on a cubic-anvil-type high-pressure apparatus. Pyrophyllite was applied as pressure transmitting medium. Once the heating time was finished, the heating power was shut down quickly, and then the pressure was slowly released to ambient pressure with a speed of 2 GPa h^{-1}.

Structure characterization: The temperature dependent (100-300 K) synchrotron x-ray diffraction was performed with a 0.01° resolution at the beamline BL02B2 in SPring-8, Japan. The measurement wavelength we used was 0.7754 Å. The GSAS program was adopted to refine the structural parameters on the basis of the Rietveld method.[1] Neutron powder diffraction measurements were carried out using the constant wavelength high resolution neutron powder diffractometer HB2a housed at the High Flux isotope reactor in Oak Ridge National Laboratory, USA. The temperature dependent diffraction profiles were measured with a wavelength λ = 2.406 Å with collimation of 12'-21'-12', before monochromator, sample and detector respectively. The sample contained in a vanadium can was cooled using a top loading cryorefrigerator. The refinements were completed by the Rietveld method with the FullProf program.[2] The selected area electron diffraction patterns were obtained using transmission electron microscope (JEOL, JEM-2100HC) operating at 200 kV equipped with a liquid-nitrogen-cooling holder.

Magnetic, specific heat, and X-ray absorption spectroscopy measurements: The temperature

dependent magnetic susceptibility and field dependent magnetization were measured by using a superconducting quantum interference device magnetometer (Quantum Design, SQUID-VSM). Both zero-field-cooling (ZFC) and field-cooling (FC) modes were used to measure the susceptibility with an applying magnetic field of 0.1 T in the temperature range between 2 K and 300 K. The magnetization data were obtained with ZFC mode at several representative temperatures. The specific heat data were collected on a physical property measurement system at zero field (Quantum Design, PPMS-9T). X-ray absorption spectroscopy measurements were carried out in Taiwan National Synchrotron Research Center at room temperature.

Dielectric constant and ferroelectric measurements: The permittivity was measured at 1 M Hz by using an Agilent-4980A LCR meter on a hard disk-shaped pellet with 2.0 mm in diameter and 0.3 mm in thickness. Silver paste was applied as electrodes. The same sample was used to measure pyroelectric current $I_p(t)$ with a Keithley 6517B electrometer when the sample was warmed up at 2 K min^{-1} from 2 K to 230 K. Before this measurement, the sample was poled with a +200 V or -200 V voltage from 200 K to 2 K, and then half hour was waited for. The ferroelectric polarization was calculated by integrating the pyroelectric current as a function of time, *i.e.* $P(t) = \int_0^t I(t)dt/S$. Here S is the area of the disk-shaped pellet, t is the time and P is the polarization. The ferroelectric hysteresis loops were measured at 20 Hz by using a Radiant Precision Premier-II Ferroelectric Test System at different temperatures based on the proposed positive-up negative-down (PUND) method.[3,4] The five voltage pulses—PN0, P1, P2, N1 and N2—used in this method. PN0 is a full loop while P1 and P2 are positive only pulses and N1 and N2 are negative only pulses. The first pulse PN0 is used to fully align FE

domains first in the positive direction and subsequently in the negative direction. During the next two positive (negative) pulses, two independent curves of effective *P* changes are recorded, and the two positive (negative) curves are subtracted from each other to produce a half *P*–*E* loop branch for $E > 0$ ($E < 0$). In this procedure, the resistive and capacitive components are subtracted out so that only the intrinsic hysteretic components are supposed to appear in the *P*–*E* loop. Therefore, the PUND method has great advantages over the conventional *P*–*E* loop scheme, particularly for polycrystalline ceramics with relatively large leakage currents.

Magnetoelectric current measurements: Magnetoelectric current was measured with a Keithley 6517B electrometer while sweeping *H* at a rate of 200 Oe s^{-1}. The change of electric polarization (ΔP) was obtained by integrating the ME current as a function of time.

Theoretical calculations: First-principles calculations for BMCO are performed using the Vienna *ab initio* Simulation Package (VASP).[5,6] The electron interactions are described using PBEsol (Perdew-Burke-Ernzerhof-revised) parametrization[7] of the generalized gradient approximation plus *U* (GGA+*U*) method[8-10]. The choice of PBEsol instead of traditional PBE can describe the solid structure better. The Hubbard U_{eff} (= *U*-*J*) which is imposed on Mn's and Cr's d orbitals using the Dudarev implementation [11] is 4 eV and 3 eV respectively.[12] The atomic positions are fully optimized iteratively until the energy converged to less than 10^{-7} eV and Hellman-Feynman forces converged to less than 0.001 eVÅ^{-1}. The plane-wave cutoff is set to 500 eV. The Monkhorst-Pack *k*-point meshes are 5×5×5. The spin-orbital coupling is not taken into account.

Table S1. Refined structure parameters of $BiMn_3Cr_4O_{12}$[a] and the bond valence sum (BVS) values for Mn and Cr based on the SXRD[b].

Parameters	300 K	100 K
a (Å)	7.39097(2)	7.38539
x(O)	0.3105(5)	0.3122(5)
y(O)	0.1758(6)	0.1776(6)
d_{Bi-O}(Å)(×12)	2.656(4)	2.652(4)
d_{Mn-O}(Å)(×4)	1.910(4)	1.909(4)
d_{Cr-O}(Å)(×6)	1.9790(14)	1.9762(15)
∠ (Cr-O-Cr)	138.13(21)	138.23(22)
BVS(Mn)	2.97	2.98
BVS(Cr)	2.88	2.91
R_{wp}(%)	5.63	5.76
R_P(%)	3.06	3.51

[a)]Space group: Im-3; Atomic sites: Bi 2*a*(0, 0, 0), Mn 6*b*(0.5, 0.5, 0), Cr 8*c*(0.25, 0.25, 0.25), and O 24*g*(*x*, *y*, 0). [b)]The BVS values (V_i) were calculated using the formula $Vi = \Sigma_j S_{ij}$, and $S_{ij} = \exp[(r_0 - r_{ij})/0.37)]$. r_0 =1.708 for Cr and 1.732 for Mn.

Table S2. Refined nuclear and magnetic structure parameters of $BiMn_3Cr_4O_{12}$ based on the NPD.

Parameters	3 K	60 K	110 K	150 K
a (Å)	7.39528(11)	7.39562(11)	7.39683(12)	7.39750(15)
x(O)	0.3117(3)	0.3111(3)	0.3108(3)	0.3109(4)
y(O)	0.1776(4)	0.1773(4)	0.1770(4)	0.1770(5)
d_{Mn-O}(Å)(×4)	1.914(3)	1.916(3)	1.916(3)	1.916(3)
d_{Cr-O}(Å)(×6)	1.978(3)	1.978(3)	1.978(3)	1.979(4)
d_{Bi-O}(Å)(×12)	2.6530(11)	2.648(2)	2.646(2)	2.646(3)
∠ (Mn-O-Mn)	103.04(10)	102.84(10)	102.73(10)	102.76(12)
∠ $(Mn-O-Cr)_1$	83.26(6)	83.15(6)	83.07(6)	83.08(8)
∠ $(Mn-O-Cr)_2$	110.70(8)	110.65(8)	110.64(8)	110.66(11)
∠ (Cr-O-Cr)	138.34(4)	138.40(4)	138.39(4)	138.36(5)
$M_{Mn}(\mu_B)$	2.31(8)	0	0	0
$M_{Cr}(\mu_B)$	2.77(5)	2.47(3)	1.20(3)	0
R_{Bragg}(%)	3.348	3.316	3.376	2.257

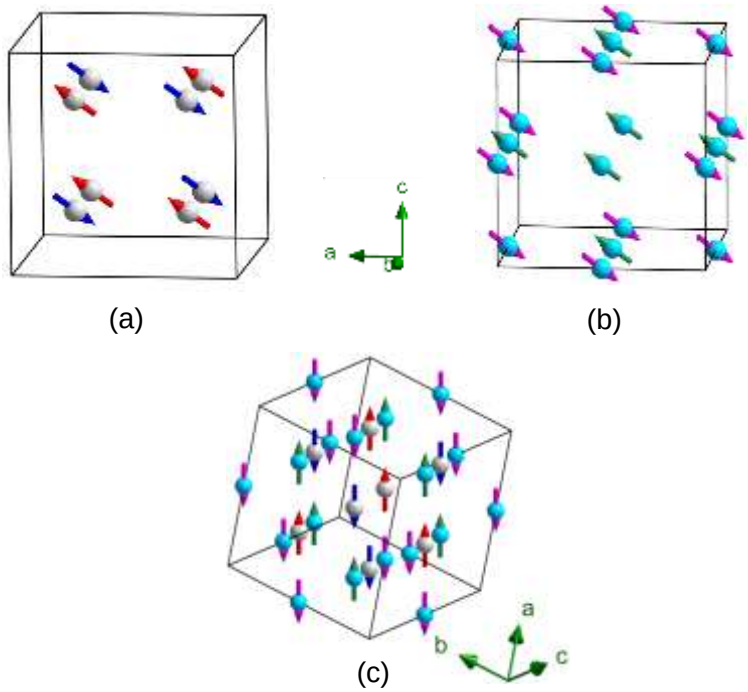

Figure S1. (a-c) The G-type AFM structure for the B-site Cr-sublattice and the A′-site Mn-sublattice with spin moment along with the crystal [111] direction, respectively. **c,** A complete set of spin alignment composed of both Cr and Mn spins below T_{N2}, giving a polar magnetic point group ***3***. For clarity, Bi and O atoms are omitted in the structures. gray ball: Cr atom; cyan ball: Mn atom.

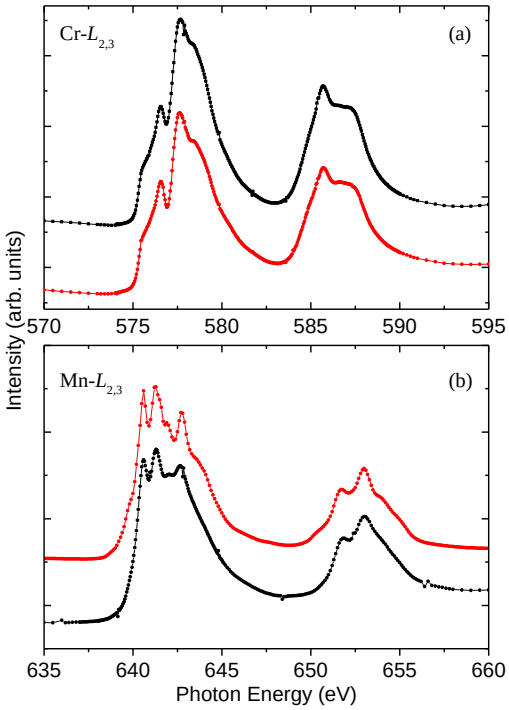

Figure S2. XAS spectra of (a) Cr-$L_{2,3}$ edges of BMCO (black) and the Cr^{3+} reference Cr_2O_3 (red) with similar CrO_6 octahedral coordination, and (b) Mn-$L_{2,3}$ edges of BMCO (black) and the Mn^{3+} reference $YMn_3Al_4O_{12}$ (red) with similar MnO_4 square-coordination environment. The similar spectral shapes and energy positions of both Cr and Mn absorption edges with those of the related references solidly confirm the Mn^{3+}/Cr^{3+} charge states in BMCO.

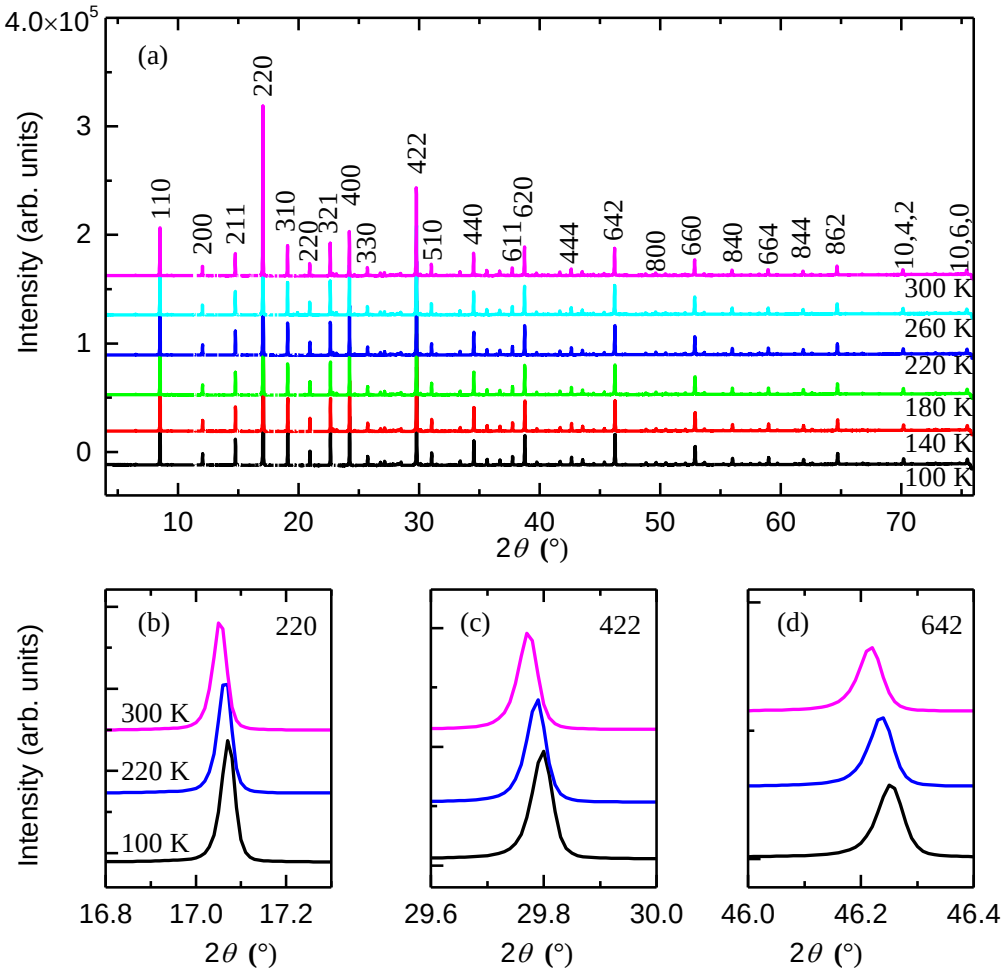

Figure S3. (a) Some representative SXRD patterns obtained from 300 K to 100 K. A small amount of impurity phases (< 5 wt%) is excluded from the patterns. (b-d) Some characteristic diffraction peaks collected at different temperatures. The diffraction peaks shift monotonically toward higher angles on cooling due to thermal contraction of the lattice, and there is no appearing/disappearing of any diffraction peak in the whole temperature region we measured. Based on these features, there is no visible long-range structural variation with decreasing temperature to 100 K.

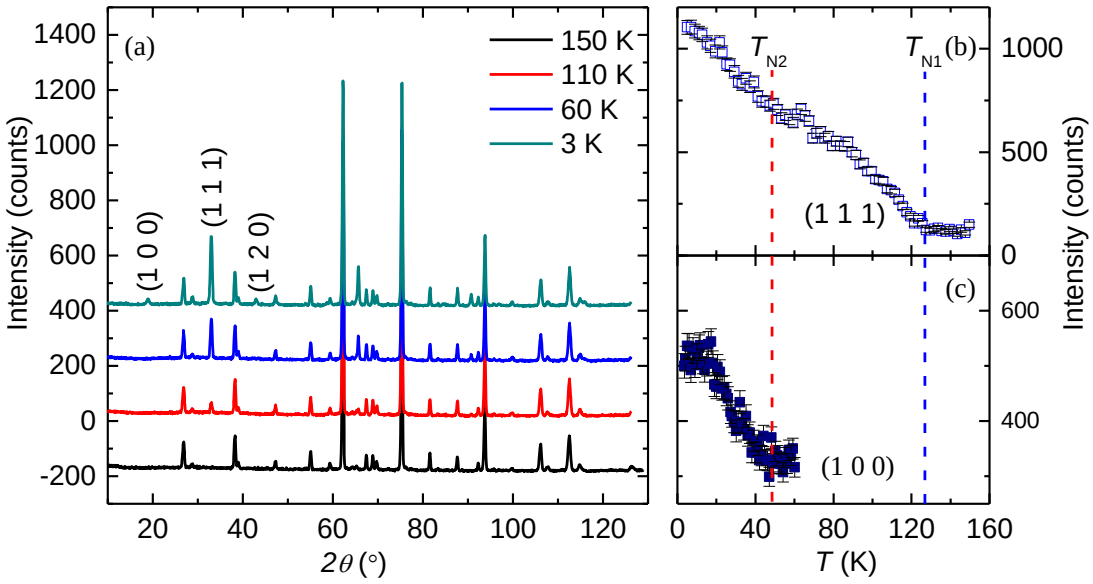

Figure S4. (a) The NPD patterns measured at selected temperatures. The AFM transitions occurring at $T_{N1} \approx 125$ K and $T_{N2} \approx 48$ K are attributed to the long-range spin orderings of the B-site Cr^{3+}-sublattice and the A′-site Mn^{3+}-sublattice, respectively. No visible macroscopic crystal structure variation is observed with temperature down to 3 K. (b,c) Temperature dependence of the integrated NPD intensities for (111) and (100) diffraction peaks, which reflect the spin orders for the B-site Cr^{3+} ions and the A′-site Mn^{3+} ions, respectively.

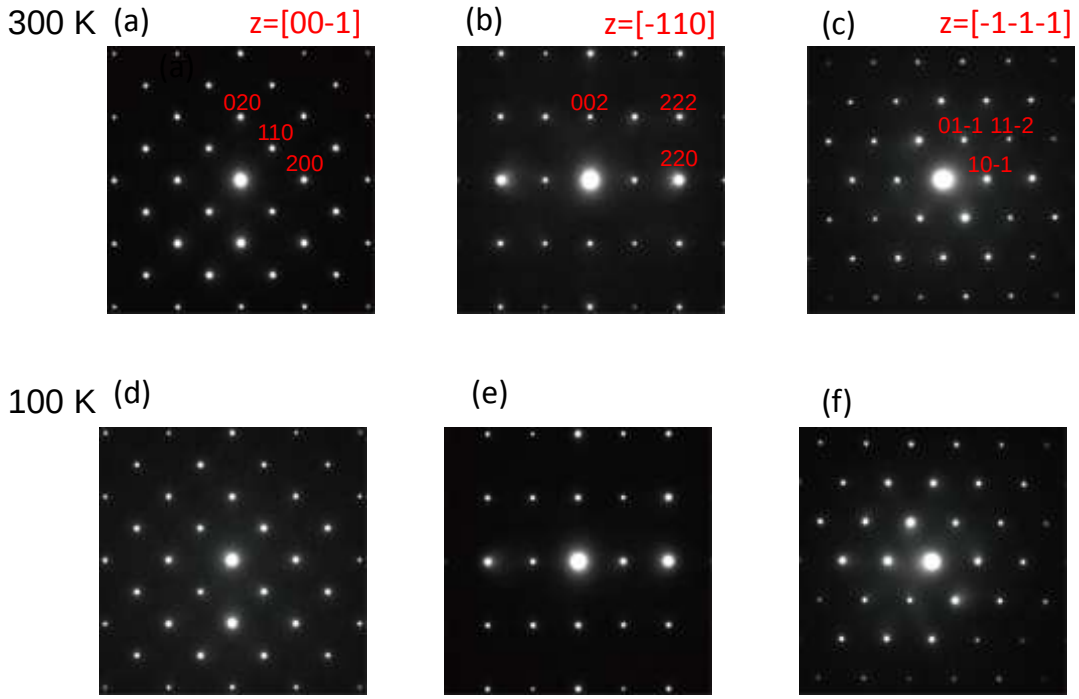

Figure S5. (a-c) Electron diffraction patterns measured at 300 K (> T_{FE1}) along with three crystal zone directions [00-1], [-110], and [1-1-1]. (d-f) The patterns measured at 100 K (< T_{FE1}) with the same directions. The patterns obtained at these two temperatures are constant, confirming the stability of the long-range crystal structure.

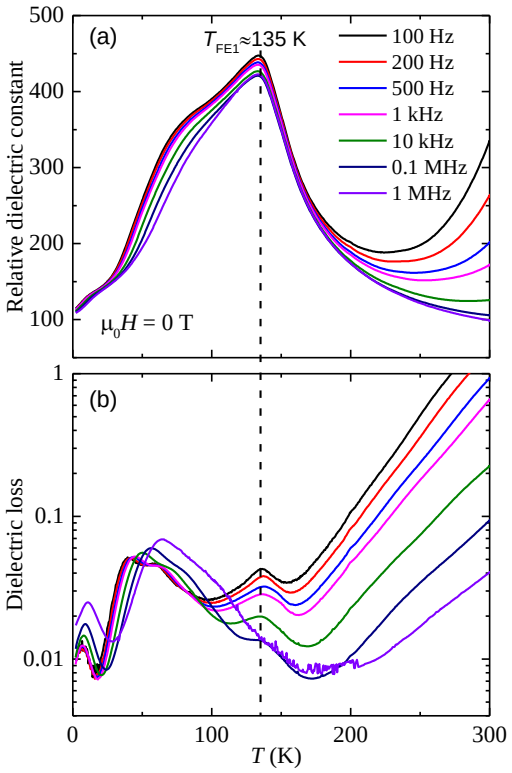

Figure S6. Temperature dependence of (a) relative dielectric constant, and (b) dielectric loss at selected frequencies.

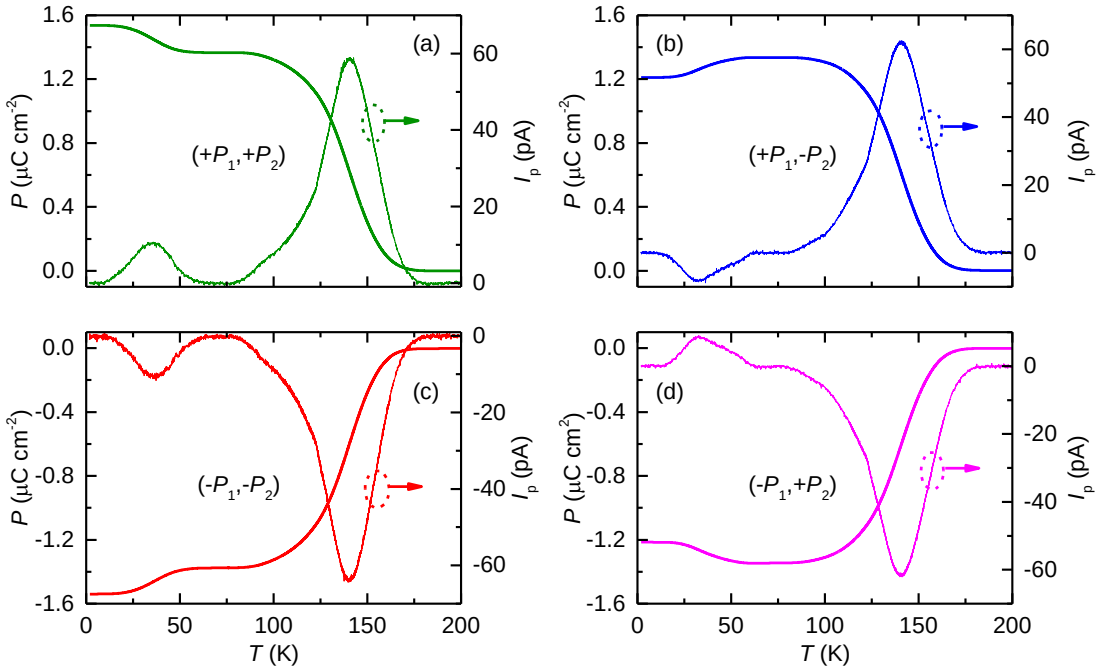

Figure S7. Temperature dependent I_p and calculated P curves under different poling procedures using the poling electric field with the magnitude of 6 kV cm^{-1}. The expected polarization states arising from the two ferroelectric phases below T_{N2}/T_{FE2} are (a) ($+P_1$, $+P_2$), (b) ($+P_1$, $-P_2$), (c) ($-P_1$, $-P_2$), (d) ($-P_1$, $+P_2$). For details, the (a) ($+P_1$, $+P_2$) state can be obtained by $+E$ poling from 200 K to 2 K; the (b) ($+P_1$, $-P_2$) state can be obtained by $+E$ poling from 200 K to 55 K, and then $-E$ poling from 55 K to 2 K; the (c) ($-P_1$, $-P_2$) state can be obtained by $-E$ poling from 200 K to 2 K; (d) the ($-P_1$, $+P_2$) state can be obtained by $-E$ poling from 200 K to 55 K, and then $+E$ poling from 55 K to 2 K.

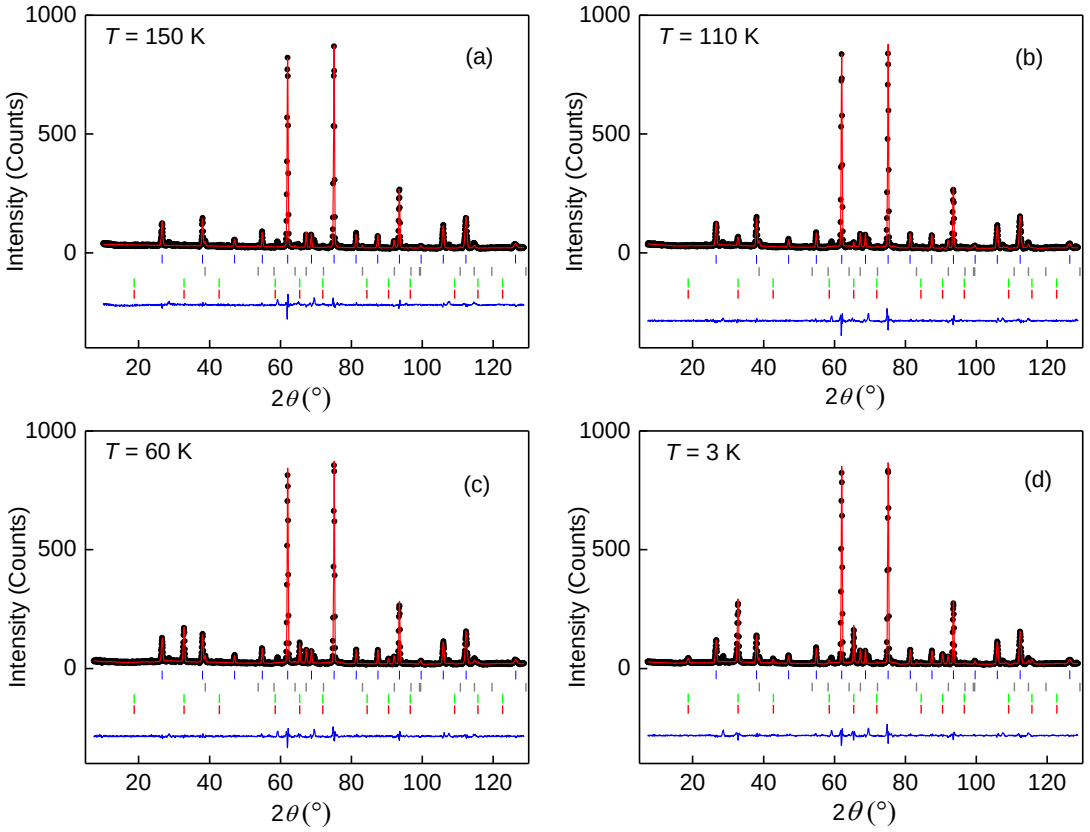

Figure S8. Rietveld refinements for the NPD data of $BiMn_3Cr_4O_{12}$ collected at 150, 110, 60, and 3 K. The observed (filled dot), calculated (red line), and difference (blue line) were shown. The ticks indicate the allowed Bragg reflections for nuclear and magnetic diffractions (blue for nuclear peaks, green for Mn magnetic peaks, and red for Cr magnetic peaks). A small amount of Cr_2O_3 impurity (< 5%) was observed.

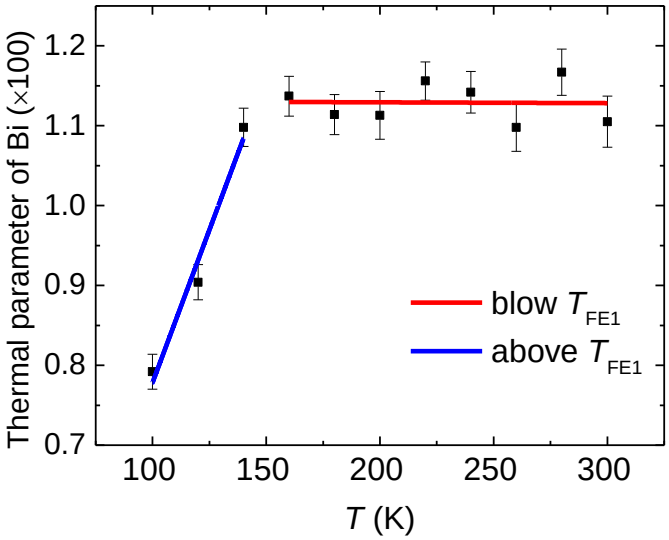

Figure S9. Temperature dependence of the thermal parameter of Bi. The solid lines are the linear fitting results. The thermal parameter of Bi is almost unchanged above T_{FE1}, whereas it sharply drops below T_{FE1}, suggesting a paraelectric-to-ferroelectric phase transition around T_{FE1}.

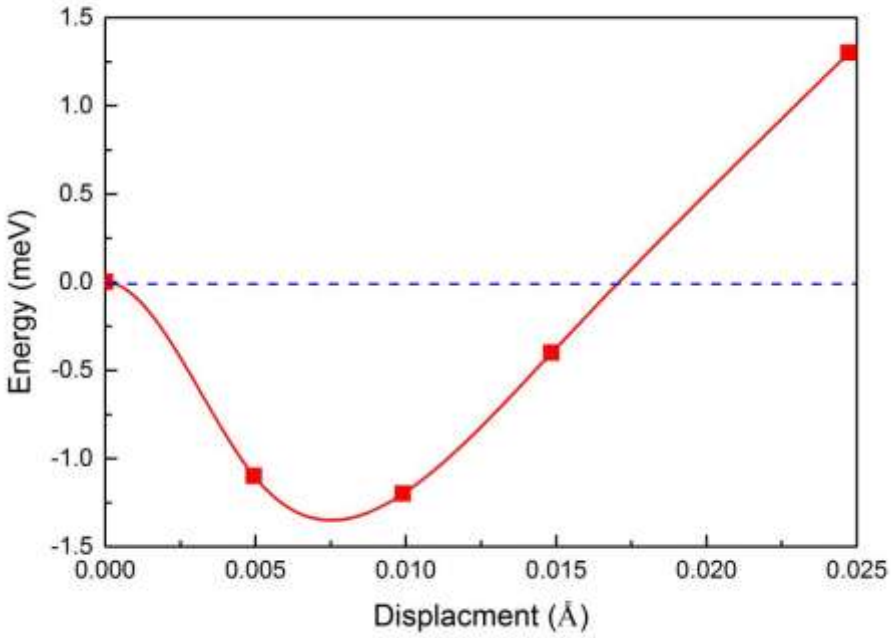

Figure S10. The calculated energy as a function of Bi's displacement. By moving all Bi ions along the *b* axis, the curve of calculated energy (per unit cell) evolves like a well, supporting the appearance of ferroelectricity. It should be noted that the depth for the energy well is only 1.3 meV, which is close to the reliable precision of DFT calculation. In this sense, more dense points for a smooth profile are beyond the reliable precision, especially near the zero displacement. Dots: calculated. Curve: fitted.

References:

1. A. C. Larson, R. B. von Dreele, *General Structure Analysis System (GSAS)*. Report No. LAUR 86-748 (Los Alamos National Laboratory, **1994**.
2. J. Rodriguezcarvajal, *Physics B* **1993**, *192*, 55.
3. J. F. Scott, L. Kammerdiner, M. Parris, S. Traynor, V. Ottenbacher, A. Shawabkeh, W. F. Oliver, *J. Appl. Phys.* 1988, *64*, 787.
4. Y. S. Chai, Y. S. Oh, L. J. Wang, N. Manivannan, S. M. Feng, Y. S. Yang, L. Q. Yan, C. Q. Jin, K. H. Kim, *Phys. Rev. B* 2012, *85*, 184406.
5. G. Kresse, J. Hafner, *Phys. Rev. B* **1993,** *47*, 558.
6. G. Kresse, J. Furthmüller, *Phys. Rev. B* **1996**, *54*, 11169.
7. J. P. Perdew, A. Ruzsinszky, G. I. Csonka, O. A. Vydrov, G. E. Scuseria, L. A. Constantin, X. L. Zhou, K. Burke, *Phys. Rev. Lett.* **2008**, *100*, 136406.
8. J. P. Perdew, K. Burke, M. Frnzerhof, *Phys. Rev. Lett.* **1996**, *77*, 3865.
9. G. Kresse, D. Joubert, *Phys. Rev. B* **1999**, *59*, 1758.
10. P. E. Blöchl, *Phys. Rev. B* **1994,** *50*, 17953.
11. S. L. Dudarev, G. A. Botton, S. Y. Savrasov, C. J. Humphreys, A. P. Sutton, *Phys. Rev. B* **1998**, *57*, 1505.
12. S. Lv, H. Li, X. Liu, J. Meng, *J. Appl. Phys.* **2011,** *110*, 023711.